Numerical and experimental study of microwave-excited microplasma and micronozzle flow for a microplasma thruster

Takeshi Takahashi,[a] Yoshinori Takao, Koji Eriguchi, and Kouichi Ono[b]
Department of Aeronautics and Astronautics, Graduate School of Engineering, Kyoto University, Yoshida-Honmachi, Sakyo-ku, Kyoto 606-8501, Japan

(Received 28 May 2009; accepted 27 July 2009; published online 20 August 2009)

Plasma and aerodynamic features have been investigated for a microplasma thruster of electrothermal type using azimuthally symmetric microwave-excited microplasmas. The thruster developed consisted of a microplasma source 1.5 mm in diameter, 10 mm long with a rod antenna on axis, and a converging-diverging micronozzle 1 mm long with a throat 0.2 mm in diameter. The feed or propellant gas employed was Ar at pressures of 10–50 kPa with flow rates of 10–70 SCCM (SCCM denotes standard cubic centimeter per minute at STP) and the surface wave-excited plasmas were established by 4.0 GHz microwaves at powers of ≤ 6 W. Numerical analysis was made for the plasma and flow properties by developing a self-consistent, two-dimensional model, where a two-temperature fluid model was applied to the entire region through the microplasma source to the micronozzle (or through subsonic to supersonic); in the former, an electromagnetic model based on the finite difference time-domain approximation was also employed for analysis of microwaves interacting with plasmas. In experiments, optical emission spectroscopy was employed with a small amount of additive gases of H_2 and N_2, to measure the plasma electron density and gas temperature in the microplasma source around the top of the microwave antenna, just upstream of the micronozzle inlet; in practice, the numerical analysis exhibited a maximum thereabout for the microwave power density absorbed, plasma density, and gas temperature. The Stark broadening of H Balmer line and the vibronic spectrum of N_2 second positive band indicated that the electron density was in the range of $(3-12)\times 10^{19}$ m^{-3} and the gas or rotational temperature was in the range of 700–1000 K. The thrust performance was also measured by using a microthrust stand with a combination of target and pendulum methods, giving a thrust in the range of 0.2–1.4 mN, a specific impulse in the range of 50–80 s, and a thrust efficiency in the range of 2%–12%. These experimental results were consistent with those of numerical analysis, depending on microwave power and gas flow rate. © *2009 American Institute of Physics*. [DOI: 10.1063/1.3205889]

I. INTRODUCTION

Small spacecraft recently attracted increasing attention in space technology to reduce the overall mission costs and greatly increase the launch rates.[1,2] Reducing the scale of spacecraft decreases the mission costs and simplifying the structure leads to short development periods. To realize microspacecraft of <10 kg (or nano-/picosatellites), their components have to be miniaturized drastically, including the propulsion system for station keeping (requiring a thrust of $\sim$mN) and for attitude control ($\sim\mu$N). Various microthrusters have been proposed for these applications,[2–6] including microelectric propulsion systems or microplasma/ion thrusters:[7–24] direct current (dc) microarcjet thruster,[7–9] dc microplasma thruster,[10] micro-Hall thruster,[11,12] micro-ion thruster,[13,14] ferroelectric plasma thruster,[15,16] and dielectric capillary discharge acceleration[17] using gas fuels; field emission electric propulsion[18] and colloid thruster[19] using liquid fuels; vacuum arc microthruster,[20] microlaser-ablation plasma thruster,[21,22] and micropulsed plasma thruster[23,24] using solid fuels. Most of these are the applications of microplasmas or microdischarges on which extensive work has recently been done. However, none of microthrusters are well established until now.

We developed a microplasma thruster of electrothermal type using azimuthally symmetric microwave-excited microplasmas,[25–31] consisting of a microplasma source and a micronozzle as shown in Fig. 1. The microplasma source is made of a dielectric chamber $\sim$1.5 mm in inner diameter and $\sim$10 mm long covered with a metal grounded, having a metal rod antenna on axis covered with a dielectric envelope, which produces high temperature plasmas at around atmospheric pressures. Note that the present configuration of microwave plasma source was originally developed for plasma material processing in large diameter,[32–35] establishing discharges relatively easily over a wide pressure range by surface waves excited around the dielectric envelope of the antenna on axis. The micronozzle concerned is a converging-diverging type (or Laval nozzle) $\sim$1 mm in length, having a throat of $\sim$0.2 mm in diameter, which converts high thermal energy of plasmas into directional kinetic energy of supersonic plasma flows to obtain the thrust. The microwave power employed would be limited to <10 W, taking into account the electric power generated by solar cell panels installed on the microspacecraft concerned.

Assuming that the plasmas are excited by surface waves,

[a]Electronic mail: t-takahashi@aero.mbox.media.kyoto-u.ac.jp.
[b]Electronic mail: ono@kuaero.kyoto-u.ac.jp.

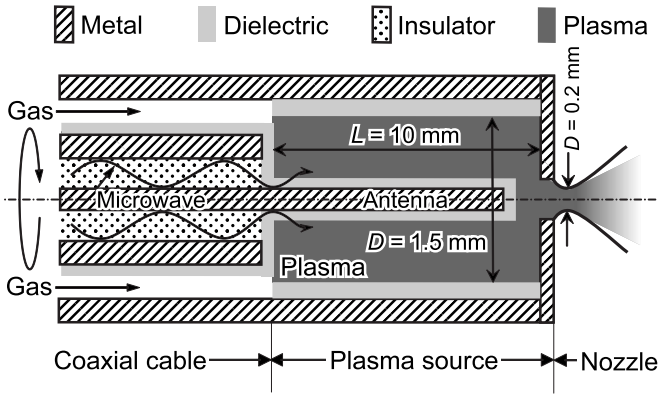

FIG. 1. Schematic of the microplasma thruster using azimuthally symmetric microwave-excited microplasmas, consisting of a microplasma source with a rod antenna on axis and a converging-diverging (Laval) micronozzle.

the major feature of our system is that microwaves penetrate into the plasma chamber along the plasma-dielectric interfaces even in the overdense mode and so the electron heating occurs in a thin (a few millimeters deep or less) skin-depth layer; that is, most of the power is absorbed near the interfaces. Such mechanism of the power deposition is a great advantage to generate plasmas in a limited space without magnetic-field confinement. These features would contribute to a simple structure and long-time operation, compared with other conventional microplasma thrusters, because the present thruster requires no electrodes, neutralizers, and magnets. This paper presents a numerical and experimental study of the microplasma thruster presently developed, with emphasis being placed on a better understanding of distinguished characteristics of the microwave-excited microplasma and micronozzle flow. A self-consistent numerical model was newly developed over the entire region of interest through microplasma source to micronozzle, taking into account the electromagnetic wave propagation, plasma evolution, and gas/plasma flow evolution from subsonic to supersonic. The working gas of interest in this study was Ar, which is an engineering model for studying plasma and fluid physics in a microplasma thruster. The numerical results were compared with the plasma density and gas temperature experimentally measured in the plasma source region by optical emission spectroscopy; a comparison was also made with the measurements of thrust performance.

II. NUMERICAL ANALYSIS

A. Model

1. General

The numerical model consisted of an electromagnetic module (EM) for microwave propagation in interacting with plasmas and a fluid module (FM) for plasma flows with two (electron and heavy particle) temperatures. The former employed the finite difference time-domain (FDTD) approximation, being applied to the microplasma source, to analyze the microwave power absorbed in the plasma. The latter employed two-temperature fluid equations, being applied to the entire region through the plasma source to micronozzle, to analyze the plasma and nozzle flow characteristics. Gas-phase reaction processes were taken into account in both regions along with plasma-wall interactions in a limited space, and the analysis of the nozzle flow finally gave the thrust performance achieved. The numerical analysis relied on the azimuthally symmetric coordinate system [two-dimensional r-z system, $\partial/\partial\theta=0$] assuming that: (i) the plasma is a two-phase medium consisting of electrons and heavy particles (ions and neutrals) and the temperature of electrons is different from that of heavy particles $[T_e \neq T_h(=T_i=T_n)]$. (ii) The plasma is macroscopically quasineutral, or the electron density equals that of ions $(n_e=n_i)$. (iii) The atomic processes in the gas phase are electron-impact excitation/de-excitation and ionization/recombination, taking into account metastable as well as ground-state atoms for neutrals. (iv) The charged particles (ions and electrons) diffuse toward the walls according to the ambipolar diffusion. (v) The sheath structures are neglected at the plasma-wall interfaces. (vi) The gas/plasma flow is laminar, and the convective velocity $\boldsymbol{v}$ is the same for all species (electrons and heavy particles). (vii) In the microplasma source, the microwave energy is absorbed by plasma electrons, which, in turn, is transferred to heavy particles through elastic collisions between them. It should be noted here that this model takes into account the gas/plasma flow self-consistency over the entire region through the microplasma source to the micronozzle (or through subsonic to supersonic), while our previous model neglected the flow in the plasma source region.[25,29,30]

2. Electromagnetic model module

The EM for the microplasma source consists of Maxwell's equations for electromagnetic fields of microwaves and equations for plasma electrons (neglecting the Lorentz force and pressure gradient):[25,34,35]

$$\nabla \times \boldsymbol{E} = -\frac{\partial \boldsymbol{B}}{\partial t}, \tag{1}$$

$$\nabla \times \boldsymbol{B} = \mu_0\left(\boldsymbol{j} + \epsilon_r\epsilon_0\frac{\partial \boldsymbol{E}}{\partial t}\right), \tag{2}$$

$$m_e\frac{\partial \boldsymbol{u}_e}{\partial t} = -e\boldsymbol{E} - m_e\nu_e\boldsymbol{u}_e, \tag{3}$$

$$\boldsymbol{j} = -en_e\boldsymbol{u}_e, \tag{4}$$

where $\boldsymbol{E}$ and $\boldsymbol{B}$ are the electric and magnetic fields of microwaves, respectively, $\boldsymbol{j}$ is the plasma current density induced by microwaves, ϵ_0 is the electric permittivity of vacuum, ϵ_r is the relative permittivity, μ_0 is the magnetic permeability of vacuum, e is the magnitude of electron charge, m_e is the mass of electron, $\boldsymbol{u}_e$ is the electron mean velocity driven by microwaves, ν_e is the effective momentum transfer collision frequency between electrons and heavy particles, and n_e is the plasma electron density. Equations (3) and (4) imply that the plasma is treated as a dielectric material of relative permittivity:

$$\epsilon_r = \epsilon_p = 1 - \frac{(\omega/\omega_{pe})^{-2}}{1 - j(\nu_e/\omega)}, \tag{5}$$

where j is the imaginary unit, ω is the angular frequency of electromagnetic waves, and $\omega_{pe}=(n_e e^2/m_e\epsilon_0)^{1/2}$ is the plasma electron frequency. Note that in the dielectric/insulator region, the current density is set to be zero ($\boldsymbol{j}=0$ or $\boldsymbol{u}_e=0$) with the permittivity ϵ_r of materials. The power absorption $\boldsymbol{j}\cdot\boldsymbol{E}$ in the plasma is taken to arise only from the classical Ohmic heating of electrons. Assuming the azimuthal symmetry of the configuration, only the transverse magnetic waves exist in the plasma chamber with $\boldsymbol{E}=(E_r,0,E_z)$ and $\boldsymbol{B}=(0,B_\theta,0)$.

The transverse electromagnetic waves are injected into the system at the excitation plane (1.2 mm upstream of the end of the coaxial cable) and the total power injected into the chamber is monitored thereat by using

$$P_{in} = \frac{1}{\mu_0}\int_A (\boldsymbol{E}\times\boldsymbol{B})dA, \tag{6}$$

where A is the cross section concerned. Mur's first-order absorbing boundary condition,

$$\frac{\partial E_r}{\partial x} - \frac{1}{c}\frac{\partial E_r}{\partial t} = 0, \tag{7}$$

is applied to the field component E_r at the left end of the coaxial cable (0.8 mm further upstream of the excitation plane), so that the electromagnetic waves propagating from the chamber to the excitation plane leave the simulation area without any artificial reflection. Here, c denotes the speed of electromagnetic waves in the insulator of the cable. Since all metallic parts are treated as perfectly conducting materials, the electric field components tangential to metal surfaces are set to be zero. The axisymmetry of the problem further implies that $E_r=0$ and $\partial E_z/\partial r=0$ on axis (at $r=0$). The total absorbed power in the plasma is calculated as

$$P_{abs} = \int_V Q_{abs}dV = \int_V \left(\frac{1}{t_p}\int_{t_p} \boldsymbol{j}\cdot\boldsymbol{E}dt\right)dV, \tag{8}$$

where t_p is the period of the electromagnetic waves, Q_{abs} the time-averaged power density absorbed, and the averaged power density absorbed per unit volume is obtained from $\bar{Q}_{abs}=P_{abs}/V$ with the plasma volume V.

3. Fluid model module

The FM for the entire region through the microplasma source to micronozzle consists of two-temperature Navier–Stokes equations and the equation of state for a two-phase medium consisting of electrons and heavy particles (ions and neutrals):[25]

$$\frac{\partial}{\partial t}\rho + \nabla\cdot(\rho\boldsymbol{v}) = 0, \tag{9}$$

$$\frac{\partial}{\partial t}(\rho\boldsymbol{v}) + \nabla\cdot(\rho\boldsymbol{v}\boldsymbol{v}) = -\nabla p + \nabla\boldsymbol{\tau}, \tag{10}$$

$$\frac{\partial}{\partial t}n_e + \nabla\cdot(n_e\boldsymbol{v}) = \nabla\cdot(D_a n_e) + \dot{n}_e, \tag{11}$$

$$\frac{\partial}{\partial t}n_* + \nabla\cdot(n_*\boldsymbol{v}) = \nabla\cdot(D_*\nabla n_*) + \dot{n}_*, \tag{12}$$

$$\frac{\partial}{\partial t}\left(\frac{3}{2}n_e k_B T_e\right) + \nabla\cdot\left(\frac{5}{2}n_e k_B T_e\boldsymbol{v}\right) = (\boldsymbol{v}\cdot\nabla)p_e - \nabla\cdot\boldsymbol{q}_e + Q_{abs} - Q_{elas} - Q_{iz,ex} - Q_{rad}, \tag{13}$$

$$\frac{\partial}{\partial t}\left(\frac{3}{2}n_h k_B T_h\right) + \nabla\cdot\left(\frac{5}{2}n_h k_B T_h\boldsymbol{v}\right) = (\boldsymbol{v}\cdot\nabla)p_h + \boldsymbol{\tau}:\nabla\boldsymbol{v} - \nabla\cdot\boldsymbol{q}_h + Q_{elas}, \tag{14}$$

$$p = p_e + p_h = n_e k_B T_e + n_h k_B T_h = n_e k_B(T_e + T_h) + n_n k_B T_h. \tag{15}$$

Equation (9) gives the overall mass continuity, where $\boldsymbol{v}$ is the convective velocity, and the total mass density is expressed as $\rho=m_e n_e+m_h n_h\approx m_h n_h$ with the mass $m_h(=m_i=m_n)$ and density $n_h(=n_i+n_n\approx n_e+n_n)$ of heavy particles. Equation (10) gives the overall momentum conservation, where p is the pressure and $\boldsymbol{\tau}$ is the stress tensor expressed as

$$\tau_{ij} = \eta\left(\frac{\partial v_i}{\partial x_j} + \frac{\partial v_j}{\partial x_i}\right) - \frac{2}{3}\eta\delta_{ij}\frac{\partial v_k}{\partial x_k}, \tag{16}$$

with the viscosity η and Kronecker delta δ_{ij}. Equation (11) gives the conservation of electrons, with the ambipolar diffusion coefficient D_a and the source term $\dot{n}_e$ for production/destruction of plasma electrons. Equation (12) gives the conservation of Ar^* metastables, where n_* is the density of Ar^* atoms (the neutral density is $n_n=n_g+n_*$ with the density n_g of ground-state Ar atoms), D_* is the diffusivity of Ar^* in Ar, and $\dot{n}_*$ is the source term for production/destruction of Ar^*. Equations (13) and (14) give the energy conservation of electrons and heavy particles, respectively, where k_B is the Boltzmann constant, p_s is the pressure, q_s is the heat flux defined as

$$\boldsymbol{q}_s = -\kappa_s\nabla T_s, \tag{17}$$

with the thermal conductivity κ_s, and Q_{abs} is the absorbed power density of microwaves in the plasma source region ($Q_{abs}=0$ in the nozzle). Here, the subscript $s=e,h$ indicates electrons or heavy particles. Moreover, Q_{elas} denotes the energy exchange due to elastic collision between electrons and heavy particles, $Q_{iz,ex}$ is the energy exchange due to the excitation/de-excitation and ionization/recombination as listed in Table I, and Q_{rad} is the radiative energy loss. The electron viscous dissipation is neglected because of its small effect as compared with other terms in the equation. Finally, Eq. (15) gives the equation of state.

In these equations, most of the transport coefficients (η, D_a, κ_s) and the energy exchange terms (Q_{elas}, Q_{rad}) were taken to be the same as before[25,35] and the diffusivity D_* was taken from Ref. 38. In the terms concerned with nonelastic collision processes $(\dot{n}_e, \dot{n}_*, Q_{iz,ex})$, the ionization and excita-

TABLE I. Inelastic electron collision processes used in the simulation (H_j is the excitation/de-excitation energy of the reaction j).

No.	Process	Reaction	H_j (eV)	Ref.
R1	Ground state ionization	$Ar+e \rightarrow Ar^+ + 2e$	15.7	36, 37
R2	Ground state excitation	$Ar+e \rightarrow Ar^* + e$	11.6	36–38
R3	Stepwise ionization	$Ar^*+e \rightarrow Ar^+ + 2e$	4.1	39
R4	Three-body recombination	$Ar^+ + 2e \rightarrow Ar + e$	−15.7	···
R5	Superelastic collision	$Ar^* + e \rightarrow Ar + e$	−11.6	···
R6	Two-body recombination	$Ar^+ + e \rightarrow Ar^* + (h\nu)$	−4.1	···

tion rates (for reactions R1–R3 in Table I) were taken from Refs. 36–39 and the rate coefficients for the reverse processes (R4–R6) were determined from the so-called principle of detailed balance.[40] The rate coefficients of forward reactions (R1–R3) are shown in Fig. 2 as a function of electron temperature T_e.

The boundary conditions employed are: (i) the feed gases enter the plasma source region at its left end through an annular spacing thereat, where the radial velocity is set to be zero, and the axial velocity is taken to be the thermal velocity at room temperature. (ii) At the nozzle exit, all the flow properties are extrapolated from the interior, although some portions of the exit flow near the nozzle wall are subsonic; in practice, the effect of ambient pressure is assumed to be very small as long as it is sufficiently low, which is normally satisfied in space. (iii) The axisymmetry of the problem implies that the radial velocity and the radial derivatives of the other flow properties (density, temperature, pressure, axial velocity, etc.) are set to be zero on axis (at $r=0$). (iv) On the walls of the plasma source and nozzle, the nonslip conditions are imposed for flow velocity and the pressure gradient normal to the walls is set to be zero. Moreover, the walls are assumed to be noncatalytic, so that the metastable density gradient normal to the walls is also taken to be zero. (v) The electron flux and electron energy flux at the plasma-wall interfaces are assumed to be given by[35]

$$\Gamma_{e\perp} = (-D_a \nabla n_e)_\perp = 0.61 n_e \left(\frac{k_B T_e}{m_i}\right)^{1/2}, \tag{18}$$

$$q_{e\perp} = (-\kappa_e \nabla T_e)_\perp = (\mathcal{E}_e + \mathcal{E}_i)\Gamma_{e\perp}, \tag{19}$$

where $\Gamma_{e\perp}$ and $Q_{e\perp}$ are the respective components of $\mathbf{\Gamma}_e$ and $\boldsymbol{q}_e$ normal to the interfaces at the sheath-presheath boundaries; $\mathcal{E}_e = 2k_B T_e$ and $\mathcal{E}_i = 0.5 k_B T_e[1+\ln(m_i/2\pi m_e)]$ are the average energy lost at the boundaries per electron and ion, respectively ($\mathcal{E}_i = 5.2 k_B T_e$ for Ar). (vi) The heavy particle temperature at the interfaces is taken to be isothermal with a wall temperature $T_w = 500$ K for the plasma source region. On the other hand, the radiative boundary condition,

$$\kappa_h \left.\frac{\partial T_h}{\partial n}\right|_w = \epsilon\sigma T_w^4, \tag{20}$$

is employed for the nozzle region, where $\epsilon = 1.0$ and $\sigma = 5.67 \times 10^{-8}$ W m^{-2} K^{-4} are the emissivity and the Stefan–Boltzmann constant, respectively, and $\partial/\partial n$ is the derivative normal to the walls.

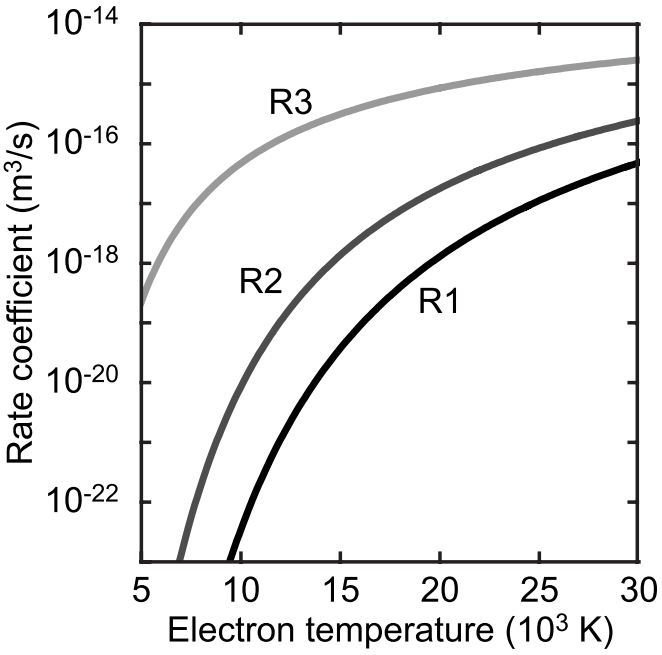

FIG. 2. Rate coefficients for electron collision processes in Ar (see Table I) as a function of electron temperature T_e.

B. Numerical procedures

In the EM for the microplasma source, Eqs. (1)–(4) were solved by using the FDTD approximation with a time increment Δt_{FDTD}. The FDTD unit cell and computational grids of the EM were similar to those used before,[25,34,35] together with the corresponding difference equations and boundary conditions. The spatial steps were taken to be $\Delta r = \Delta z = 0.01$ mm in the source region, where the simulation area was divided into 1350 cells in the axial direction and 240 cells in the radial direction at regular intervals using rectangular cells.

In the FM for the entire region through the microplasma source to micronozzle, Eqs. (9)–(15) were all discretized in a finite difference manner and the discrete equations were solved by using an implicit lower-upper symmetric Gauss–Seidel scheme with a time increment $\Delta t_{\mathrm{Fluid}}$.[41] The fluid unit cell and computational grids of the FM in the plasma source region were taken to be the same as those of the EM, being rectangular as mentioned above; on the other hand, the grids of the FM in the nozzle region were curvilinear, being the same as those used before.[25] In practice, the simulation area of the nozzle was divided into 81 cells in the axial direction with the grid spacing being finer near the throat and 30 cells in the radial direction at regular intervals, as shown in Fig. 3.

It is expected that the high-frequency perturbations of electromagnetic waves are separated from the ambipolar electric fields governed by relatively slow plasma and fluid evolution, because the characteristic timescale for the latter is much longer than that for the former. Thus, a self-consistent solution was obtained by applying the different timescale integration to the two modules of EM and FM, as in Ref. 35: (i) first, the microwave input power P_{in} and the gas injection flow rate are give to the system, together with the electron $n_e(r,z)$, metastable $n_*(r,z)$, and neutral $n_n(r,z)$

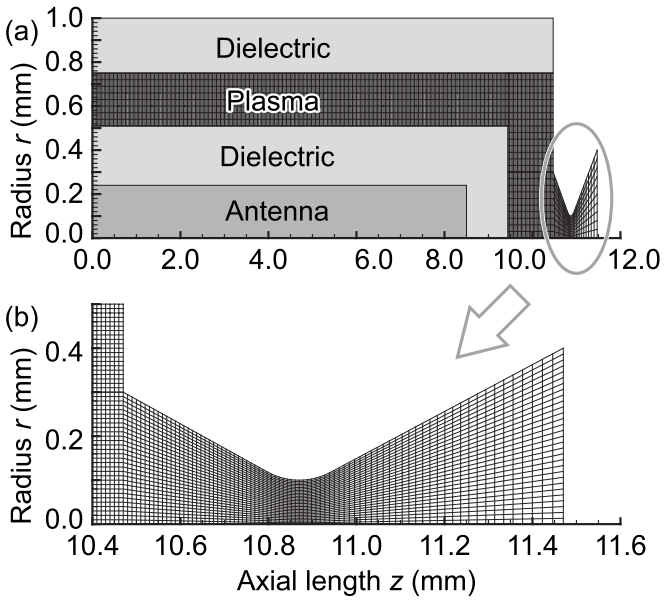

FIG. 3. (a) Cross-sectional view and computational grids for the microplasma source and micronozzle regions and (b) an enlarged view of the nozzle region.

densities, the flow velocity $\boldsymbol{v}(r,z)$, and the electron $T_e(r,z)$ and heavy particle $T_h(r,z)$ temperatures. Then, the electromagnetic fields of microwaves injected are calculated in the EM, with a time increment $\Delta t_{\mathrm{FDTD}}(=4.5\times10^{-14}$ s) for a time span T_{FDTD} of typically several microwave periods. (ii) The absorbed power density $Q_{\mathrm{abs}}(r,z)$ in the plasma source region is calculated at the end of the EM calculation, which is an input to the FM. (iii) Then, the plasma and fluid evolution is traced by the FM in the entire region through the plasma source to nozzle with a time increment $\Delta t_{\mathrm{Fluid}}(=1.5\times10^{-11}$ s) for a time span $T_{\mathrm{Fluid}}(\gg T_{\mathrm{FDTD}})$, to give the distribution of the plasma and fluid parameters in both the plasma source and nozzle. (iv) At the end of the FM calculation, the instantaneous distribution of the plasma and fluid parameters are given to the EM. These procedures (i)–(iv) are repeated until the plasma and fluid properties converge in the entire region of plasma source and nozzle to finally also give the thrust performance.

C. Numerical results

Figures 4(a)–4(h) show the spatial distribution of the electron density n_e, electron temperature T_e, heavy particle temperature T_h, absorbed power density Q_{abs}, pressure p, axial flow velocity u, Ar ground-state density n_g and Ar metastable state density n_* in the microplasma source, respectively, calculated for an input power $P_{\mathrm{in}}=6.0$ W of $f=4$ GHz microwaves, Ar mass flow rate $\dot{m}=1.5$ mg/s [flow rate of 50 SCCM (SCCM denotes standard cubic centimeter per minute at STP)], and quartz chamber and envelope ($\epsilon_d=3.8$). The absorbed power calculated in the plasma is $P_{\mathrm{abs}}=5.0$ W in total, corresponding to the average power density $\bar{Q}_{\mathrm{abs}}=6.3\times10^8$ W/m^3. Note that the microwave power not absorbed in the plasma is reflected and/or passing through the source-nozzle boundaries to leave the simulation area. The plasma density n_e exhibits its maximum near the end of the dielectric envelope of the antenna ($n_e\approx1.4\times10^{20}$ m^{-3}), being consistent with the distribution of the absorbed power density Q_{abs}. On the other hand, the heavy particle temperature T_h exhibits its maximum in a space between the end of the dielectric envelope and the end wall of the dielectric plasma source chamber ($T_h\approx880$ K), where the micronozzle is located to achieve the aerodynamic acceleration of high temperature plasmas. Such distribution of the gas temperature is preferred for a thruster of electrothermal type using a Laval nozzle (or a converging-diverging nozzle), because the plasma thermal energy should be converted into directional kinetic energy of the supersonic flow without any undesirable energy loss in the plasma source region before entering the nozzle. In addition, the pressure calculated was almost uniform in the plasma source ($p\approx34$ kPa) and the flow velocity was increased in the axial direction toward the end of the source region (up to $u\approx40$ m/s).

Also shown in Figs. 4(i) and 4(j) are snapshots of the distribution of the radial E_r and axial E_z electric fields of microwaves. The corresponding extended views of the electric fields in the dielectric as well as in the plasma are also shown in Figs. 5(a) and 5(b). These results indicate that the strength of E_r is more than ten times smaller than that of E_z in the plasma, while the former is about ten times larger than the latter in the dielectric. Moreover, the peak position of the absorbed power density Q_{abs} corresponds to that of E_z (not E_r), implying that the axial E_z is the major component of microwave electric fields that contributes to Q_{abs} and thus to P_{abs}. It should be noted here that the present two-dimensional numerical analysis, which takes into account the spatially nonuniform plasma distribution in the microplasma source, gives a high absorption efficiency $P_{\mathrm{abs}}/P_{\mathrm{in}}>80\%$ even for microwaves of low frequencies ($f=4$ GHz). This is in contrast with the results of our previous numerical study assuming the spatially uniform plasma distribution in the source,[25] being ascribed to the localized absorption of microwaves or inhomogeneous heating of electrons in the interaction of electromagnetic waves with nonuniform plasmas. In practice, the strength of E_z in the plasma is largest near the plasma-dielectric interfaces, further increasing with increasing axial distance downstream toward the end of the antenna or dielectric envelope, as can be seen in Figs. 4(j) and 5(b). Numerical results also indicated that the microwave power absorbed does not rely significantly on microwave frequency f and relative permittivity ϵ_d of dielectrics, but rely significantly on the configuration of the microplasma source (e.g., chamber length and diameter, antenna length and diameter); however, at high frequencies ($f>20$ GHz) and permittivities ($\epsilon_d>10$), the distribution of Q_{abs} (and also E_r and E_z) was found to be more localized at the plasma-dielectric interfaces, because the surface waves tend to be established thereat.[25]

Figures 6(a)–6(h) show the distribution of the electron density n_e, electron temperature T_e, heavy particle temperature T_h, Mach number Ma, pressure p, axial flow velocity u, Ar ground-state density n_g, and Ar metastable-state density n_* in the micronozzle, respectively, obtained in the same numerical simulation as Figs. 4 and 5. Here, the Mach number

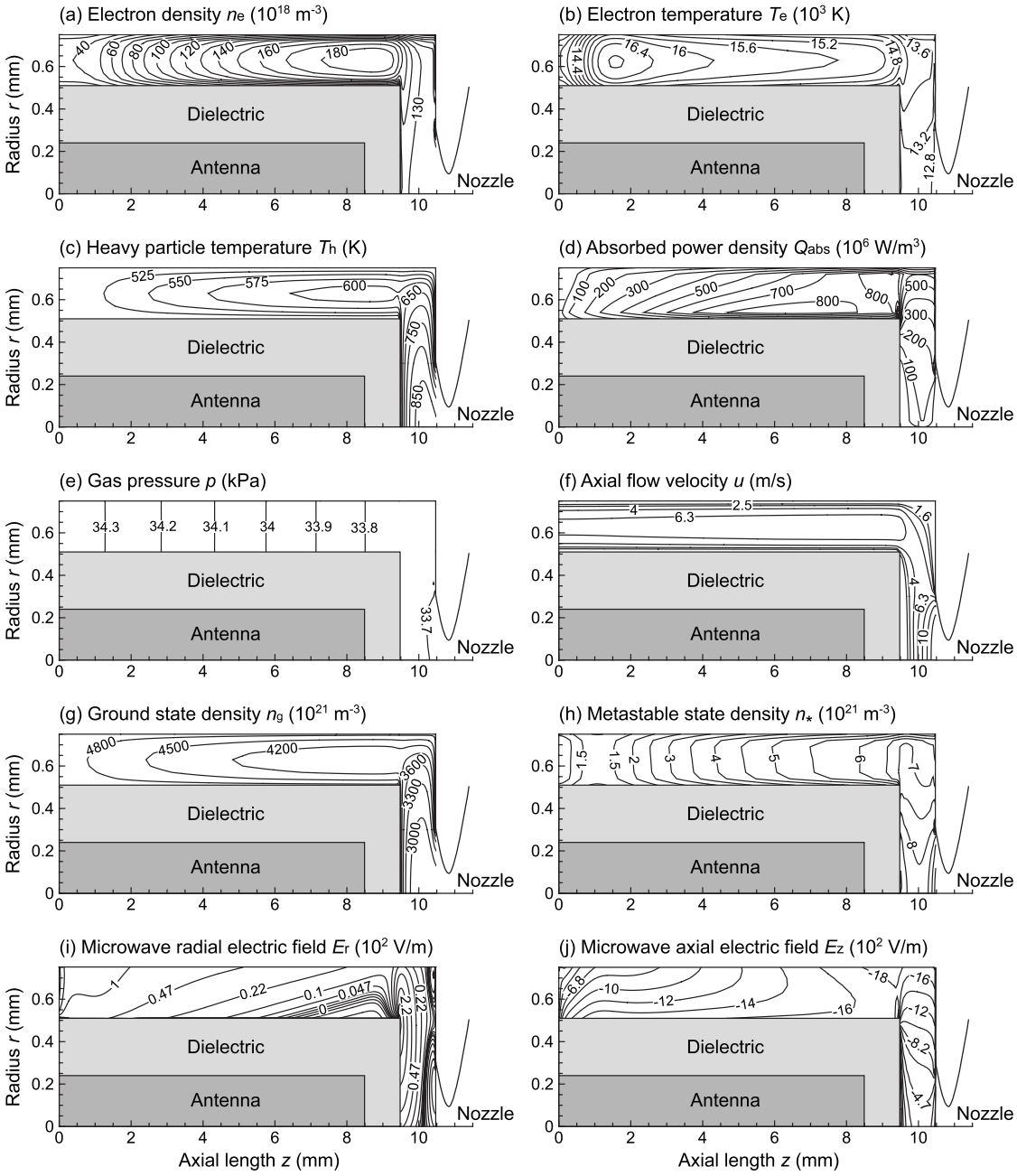

FIG. 4. Distribution of the (a) electron density n_e, (b) electron temperature T_e, (c) heavy particle temperature T_h, (d) absorbed power density Q_{abs}, (e) gas pressure p, (f) axial flow velocity u, (g) Ar ground-state density n_g, and (h) Ar metastable-state density n_* in the microplasma source, calculated for an input power P_{in}=6.0 W of f=4 GHz microwaves, Ar mass flow rate $\dot{m}$=1.5 mg/s (flow rate of 50 SCCM), and quartz chamber and envelope (ϵ_d=3.8). Here, the diameter and length of the antenna are d_{an}=0.48 mm and L_{an}=8.5 mm, respectively. The inner diameter, outer diameter, and length of the dielectric envelope covering the antenna are $d_{d,\mathrm{in}}$=d_{an}=0.48 mm, $d_{d,\mathrm{out}}$=0.96 mm, and L_d=9.5 mm, respectively. The inner diameter, outer diameter, and length of the dielectric chamber of the microplasma source are $d_{s,\mathrm{in}}$=1.44 mm, $d_{s,\mathrm{out}}$=3.0 mm, and L_s=10.5 mm, respectively. The microwave power absorbed in the plasma was calculated as P_{abs}=5.0 W. Also shown is a snapshot of the distribution of the (i) radial E_r and (j) axial E_z electric fields of the microwaves in the microplasma region.

is given by $\mathrm{Ma}=|\boldsymbol{v}|(\gamma k_B T_h/m_h)^{-1/2}$, where $\gamma=5/3$ is the specific heat ratio for monoatomic gases. The temperature T_h, Mach number Ma, pressure p, and axial velocity u exhibit a characteristic of the subsonic-supersonic flow in the converging-diverging nozzle: Ma and u increase with increasing axial distance, with Ma=1 being at around the throat, while T_h and p decrease downstream along the nozzle axis. However, the contour of Ma and u indicates that the boundary layer associated with viscosity is relatively thick in the micronozzle flow, especially in the divergent or supersonic portion of the nozzle.[25] In practice, the flow is supersonic around the nozzle axis therein, while subsonic near the walls over roughly half of the nozzle cross section. Note that the decrease in the temperature T_h along the axis is not so significant as compared to that of p, Ma, and u, owing to heating due to viscous dissipation in thick boundary layers. It is further noted that the plasma density n_e decreases downstream along the nozzle axis, which is similar to the behavior

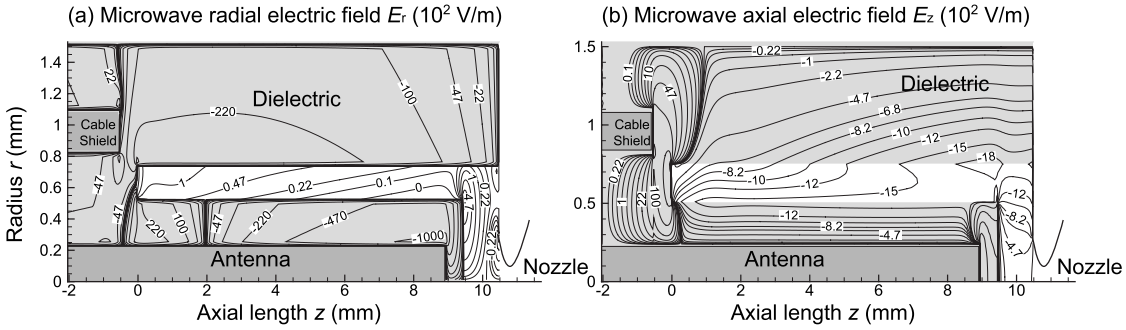

FIG. 5. Extended view of a snapshot of the distribution of the (a) radial E_r and (b) axial E_z electric fields of microwaves in the microplasma source, corresponding to Figs. 4(i) and 4(j). The figure includes the region of coaxial cable for microwave injection and the region of dielectric material containing the plasma. Note that the excitation plane for microwave injection in the numerical analysis is at $z=-1.2$ mm and the boundary for Mur's first-order absorbing condition is at $z=-2$ mm.

of the pressure p and mass density $\rho(\approx n_g)$; on the other hand, the electron temperature T_e exhibits no significant change along the axis, owing to the energy gained by plasma electrons through inelastic processes of electron-impact de-excitation and electron-ion recombination during expansion.

Figures 7 and 8 show the contour of plasma and flow properties in the microplasma source and micronozzle, respectively, for a reduced Ar mass flow rate of $\dot{m}=0.45$ mg/s (flow rate of 15 SCCM), calculated with the other parameters being the same as in Figs. 4–6. A compari-

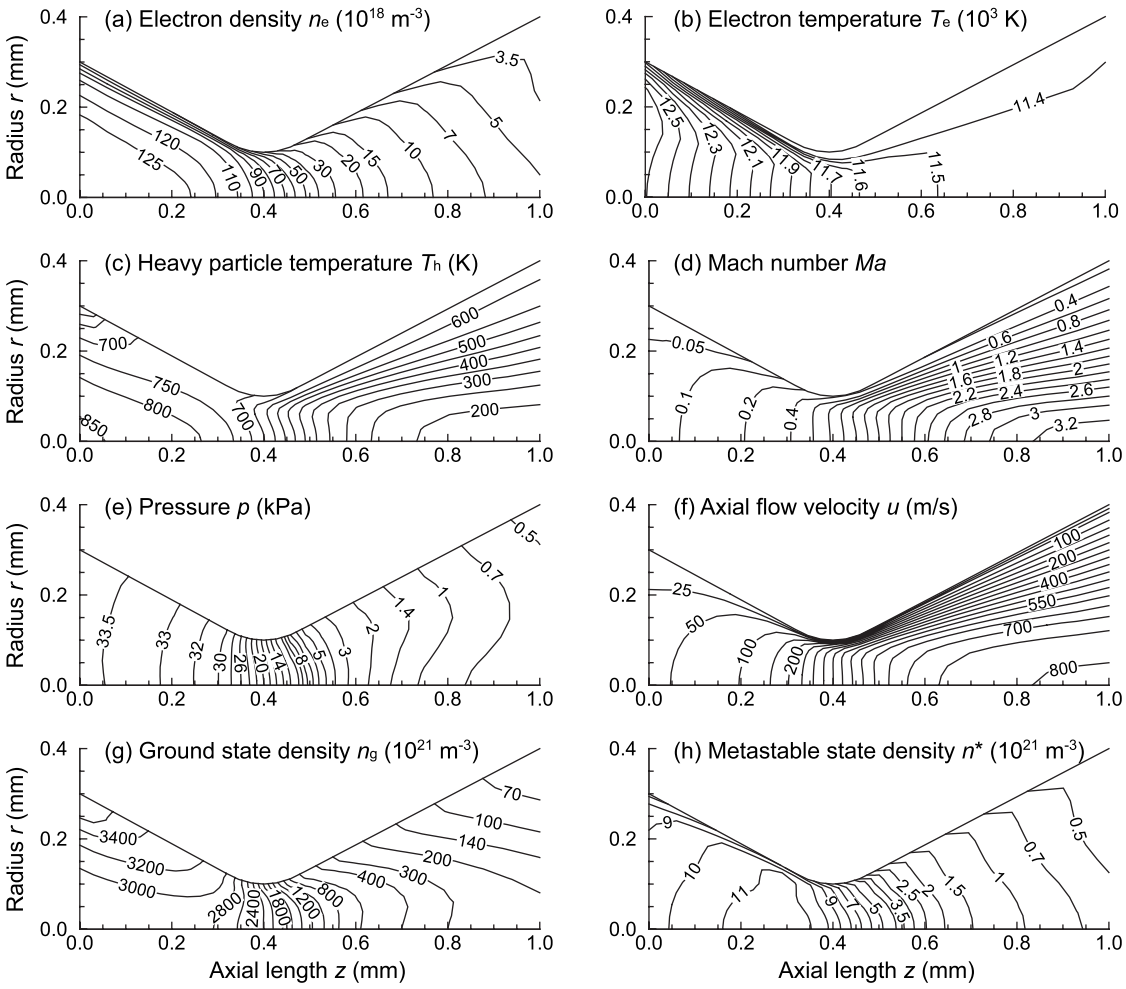

FIG. 6. Distribution of the (a) electron density n_e, (b) electron temperature T_e, (c) heavy particle temperature T_h, (d) Mach number Ma, (e) pressure p, (f) axial flow velocity u, (g) Ar ground-state density n_g, and (h) Ar metastable-state density n_* in the micronozzle, obtained in the same numerical simulation as Figs. 4 and 5. The nozzle shown has an inlet, throat, and exit diameter of $d_{in}=0.6$ mm, $d_{th}=0.2$ mm, and $d_{ex}=0.8$ mm, respectively, with a diverging angle of $\theta=26.6°$ and a total length of 1 mm.

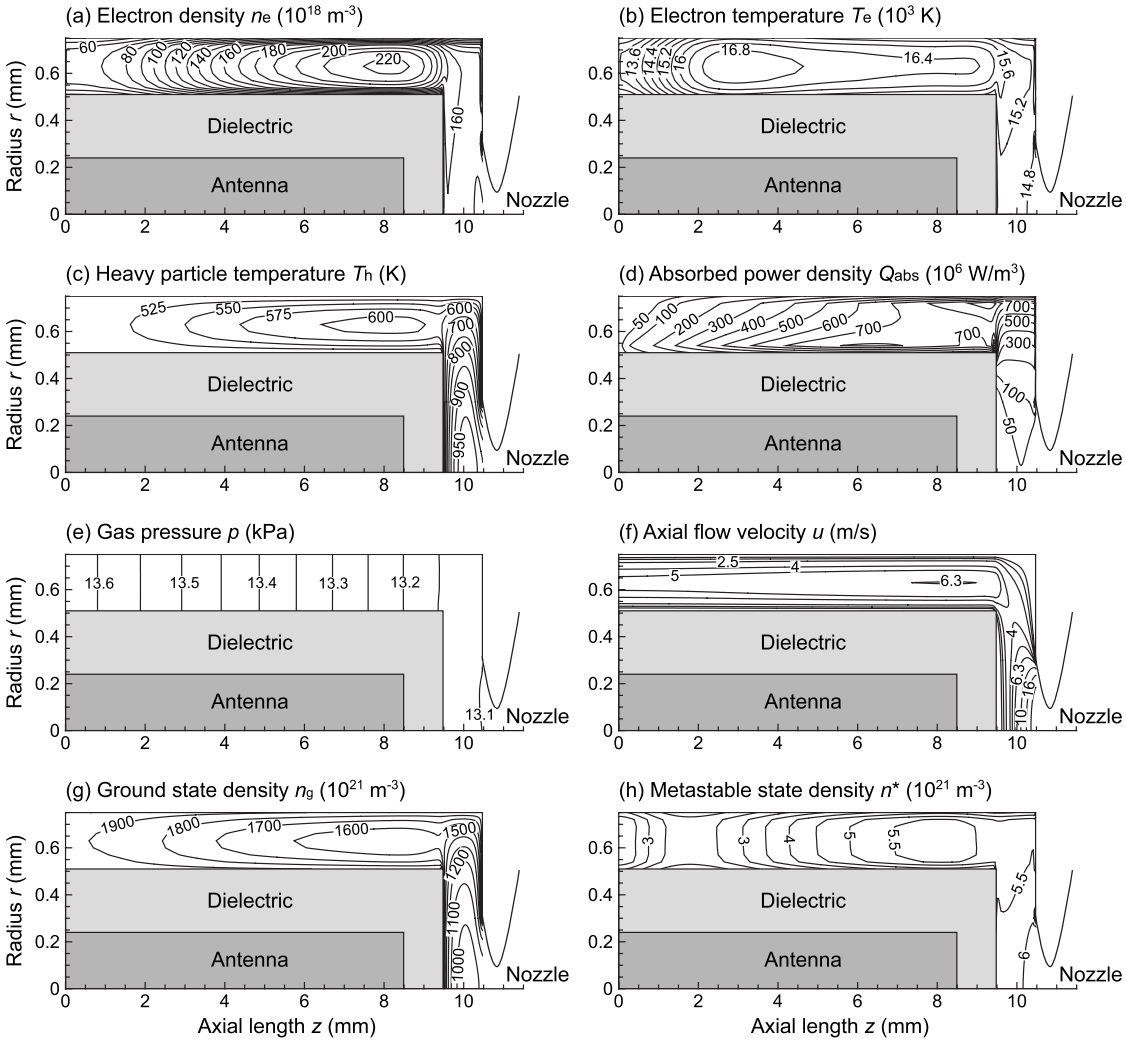

FIG. 7. Distribution of the (a) electron density n_e, (b) electron temperature T_e, (c) heavy particle temperature T_h, (d) absorbed power density Q_{abs}, (e) gas pressure p, (f) axial flow velocity u, (g) Ar ground-state density n_g, and (h) Ar metastable-state density n_* in the microplasma source for an Ar mass flow rate $\dot{m}$=0.45 mg/s (or a flow rate of 15 SCCM), calculated with the other parameters being the same as Figs. 4–6. The microwave power absorbed in the plasma was calculated as P_{abs}=5.0 W.

son of the temperature T_h, Mach number Ma, and flow velocity u in the micronozzle between Figs. 6 and 8 indicate that although significant boundary layers occur at both flow rates, the layer tends to be thicker at 0.45 mg/s than at 1.5 mg/s in the divergent portion of the nozzle. In practice, the minimum T_h and the maximum Ma and u are observed inside the micronozzle, not at the nozzle exit, at low 0.45 mg/s. Thus, it follows that, at lower gas flow rates, the thicker boundary layers impede the flow expansion in the micronozzle, where the nozzle flow is heavily underexpanded to decelerate the supersonic flow downstream along the axis in the diverging portion of the nozzle. The thicker boundary layers at lower flow rates are attributed to higher T_h thereat [see Figs. 6(c) and 8(c)]; in effect, the viscosity is a function of temperature T_h, increasing with increasing T_h, which in turn leads to higher viscous dissipation and thus to further increased T_h. The higher T_h at lower flow rates in the micronozzle originate from higher T_h achieved around the end of the antenna in the microplasma source region, as can be seen in Figs. 4(c) and 7(c), where lower pressure p or density n_g with similar values of the absorbed power density Q_{abs} would result in higher T_h.

Such boundary layer effects were also observed at high input and thus absorbed powers (high P_{in} and thus P_{abs} or Q_{abs}), where the micronozzle flow is heavily affected by viscous dissipation in boundary layers owing to the high temperature T_h of heavy particles. It should be concluded that the gas/plasma flow in the microplasma source and micronozzle is often heavily affected by the effects of boundary layers at the wall; especially in the micronozzle, the thickness of boundary layers tends to be comparable to the nozzle radius, and the viscous dissipation in boundary layers often affects the flow properties, aerodynamic acceleration of the flow, and thus thrust performance.

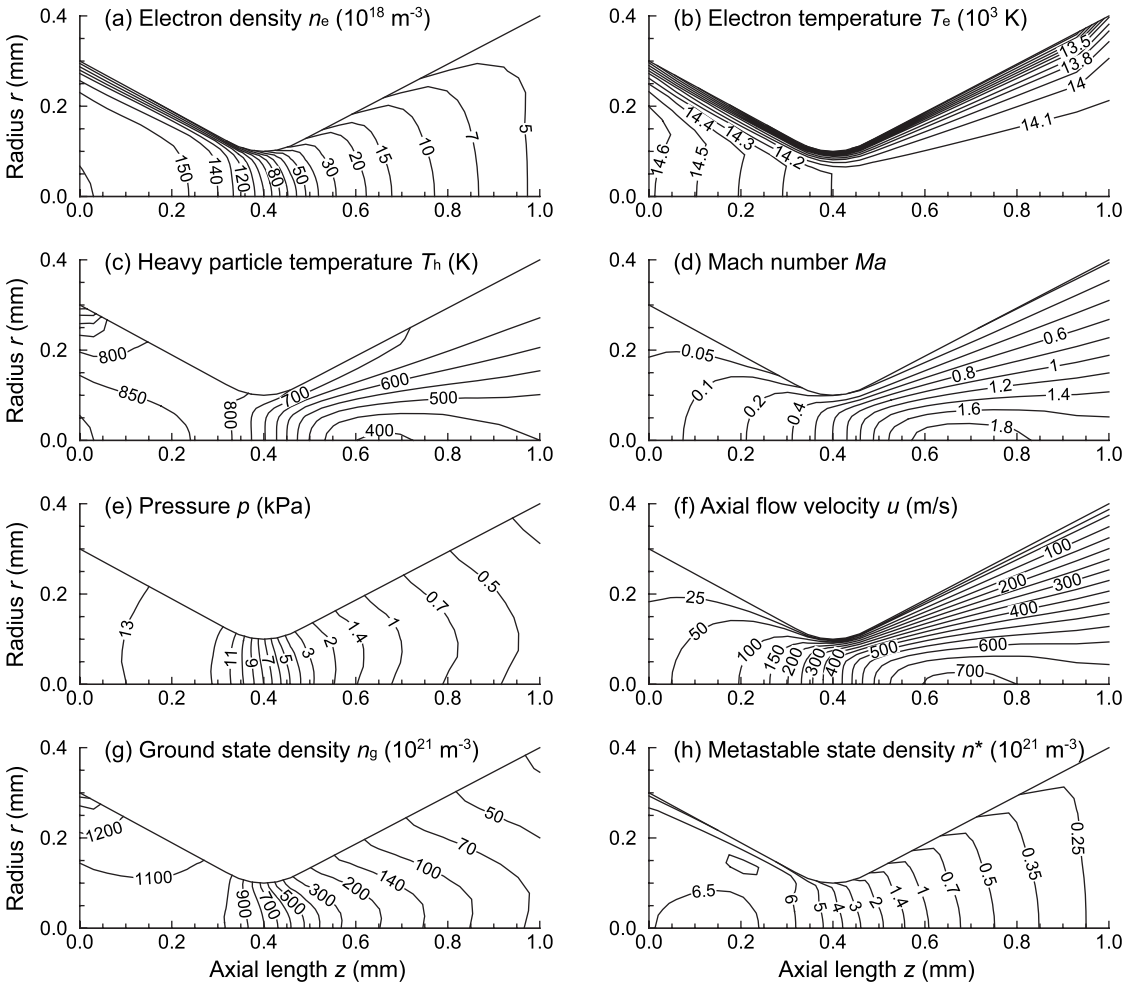

FIG. 8. Distribution of the (a) electron density n_e, (b) electron temperature T_e, (c) heavy particle temperature T_h, (d) Mach number Ma, (e) pressure *p*, (f) axial flow velocity *u*, (g) Ar ground-state density n_g, and (h) Ar metastable-state density n_* in the micronozzle, obtained in the same numerical simulation as Fig. 7.

III. EXPERIMENT

Figure 9 shows a schematic of the experimental setup.[27,28,30] The microplasma source chamber was made of a quartz tube L_s=10.5 mm long, $d_{s,\mathrm{in}}$=1.5 mm in inner diameter, and $d_{s,\mathrm{out}}$=3.0 mm in outer diameter. The center conductor of a semirigid coaxial cable (RG-405/U), protruding 10 mm beyond the insulator and outer conductor, was covered with a dielectric envelope, which was then inserted in the source chamber as a microwave antenna L_{an}=8.5 mm long and d_{an}=0.5 mm in diameter. The dielectric envelope of quartz covering the antenna was L_d=9.5 mm long, $d_{d,\mathrm{in}}$=0.5 mm in inner diameter, and $d_{d,\mathrm{out}}$=1.0 mm in outer diameter. The plasma source chamber and antenna were inserted into a stainless-steel housing to cover the microplasma source with a metal grounded, where an annular spacing was retained for feeding the fuel gas. The microplasma source thus configured was located in a vacuum chamber pumped down by a dry and turbomolecular pump.

Microwave signals of f=4 GHz from a signal generator (Agilent 8648D) were amplified through a four-stage semiconductor amplifier to powers of nominally $P_{\mathrm{in}}<10$ W and then fed into the microplasma source through the semirigid coaxial cable. The working gas was Ar in this study, being supplied through a mass flow controller; in some cases, a small amount (<5%) of N_2 and H_2 was added for plasma diagnostics. The feed gas pressure p_0 in the microplasma source was measured by a pressure gauge set upstream of the source chamber. Here, the reflection of microwaves was suppressed by adjusting the length of the coaxial cable and antenna.

Figure 10(a) shows a microscope image of the micronozzle fabricated in a 1-mm-thick quartz plate by using a micromachining process with a diamond drill.[28,30] The nozzle shown has an inlet, throat, and exit diameter of d_{in}=0.6, d_{th}=0.2, and d_{ex}=0.8 mm, respectively, being similar to the nozzle configuration of Figs. 6 and 8; the micronozzle was attached to one end of the microplasma source chamber, as shown in Fig. 9. Plasma discharges gave an elongated plume of supersonic plasma jet freely expanded downstream of the nozzle exit into vacuum, as can be seen in a photograph image shown in Fig. 10(b) (f=4 GHz, P_{in}=6 W, $\epsilon_d \approx 3.8$, Ar 50 SCCM, p_0=31 kPa); the length of the plasma jet plume was observed to increase with increasing microwave input power P_{in} and gas flow rate. In addition, the jet plume was observed to have a system of shocks therein (barrel shock at the sides and Mach disk shock normal to the cen-

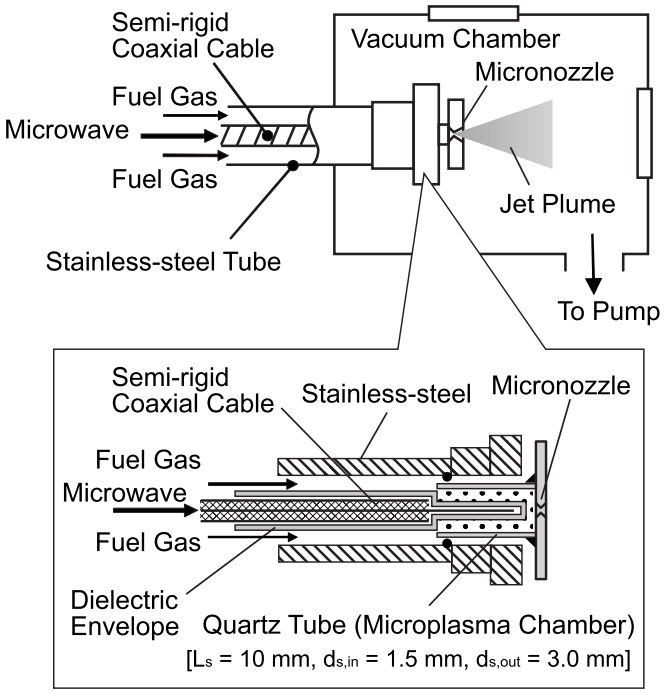

FIG. 9. Experimental setup, together with an enlarged view of the microwave- excited microplasma source having a configuration and size similar to those shown in Figs. 4, 5, and 7. Here, the dielectric envelope was also made of quartz. Optical emission spectroscopy was employed in the side-view direction, through a small hole of the stainless-steel housing around the end of the antenna or dielectric envelope, just upstream of the micronozzle inlet (Ref. 28).

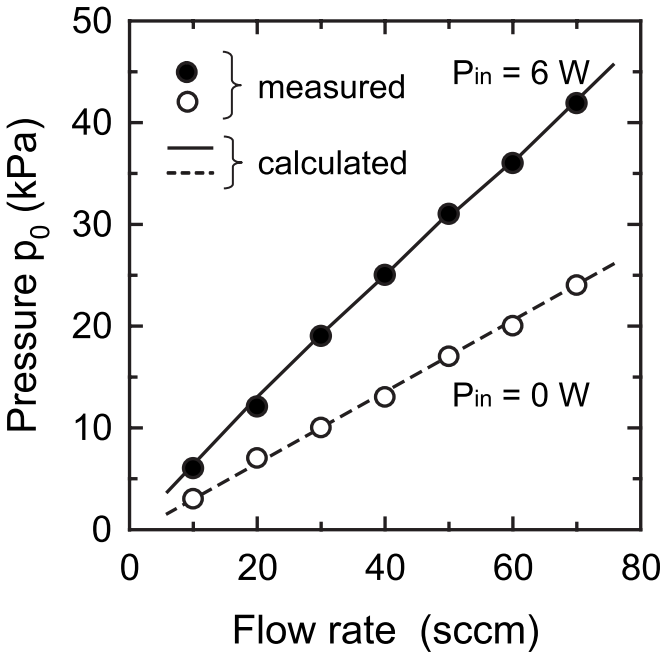

FIG. 11. Source pressure p_0 measured as a function of gas flow rate (or mass flow rate $\dot{m}$) with and without plasma discharge (f=4 GHz, P_{in}=6 W, $\epsilon_d \approx 3.8$). Also shown are the curves calculated based on the quasi-one-dimensional nozzle flow equation for an isentropic flow of perfect gases in a converging-diverging nozzle, assuming the so-called choked flow condition at the throat. Here, the gas/plasma temperature T_0 in the microplasma source was taken to be the room temperature in cold gas operation and the gas/rotational temperature spectroscopically measured in plasma discharge (as will be shown in Fig. 13).

terline), indicating a supersonic free-jet expansion through an orifice or nozzle into vacuum.[42]

The gas flow rate (or mass flow rate $\dot{m}$) and the source pressure p_0 measured with and without plasma discharge were approximately related by the quasi-one-dimensional nozzle flow equation for an isentropic flow of perfect gases in a converging-diverging nozzle,[43,44]

$$\dot{m} = \rho u A = p_0 A^* \left[\frac{\gamma}{RT_0} \left(\frac{2}{\gamma+1} \right)^{(\gamma+1)/(\gamma-1)} \right]^{1/2}, \tag{21}$$

as shown in Fig. 11. The equation assumes the so-called choked flow, or the sonic velocity, at the throat followed by further increase in velocity under supersonic flow conditions in the divergent portion of the nozzle. Here, ρ is the mass density, u is the flow velocity, A is the cross section of the nozzle, A^* is that of the throat, γ is the specific heat ratio (γ=5/3 for Ar), R is the universal gas constant ($R=k_B/m_h$), and T_0 is the gas/plasma temperature in the microplasma source. The temperature T_0 was taken to be the room temperature in cold gas operation and the gas/rotational temperature spectroscopically measured in plasma discharge (as will be shown below in Sec. IV).

To characterize the microplasma concerned, the optical emission from the plasma was observed in the side-view direction through a 1-mm-diameter small hole of the stainless-steel housing around the end of the antenna or dielectric envelope (just upstream of the micronozzle inlet).[28] The spectrometer employed consisted of a 50 cm focal length spectrograph/monochromator (Acton SpectraPro 2500i) with a grating of 2400 lines/mm, charge-coupled device detector (Princeton PI-MAX1K; 1024×1024 pixels, 13.3×13.3 mm^2), and photomultiplier (Hamamatsu R2949); a set of lenses was used to collect the emission from the plasma and focus it onto the entrance slit of the spectrometer. The spectral resolution, determined using a low-pressure Ar discharge lamp, was 0.025 nm with an entrance

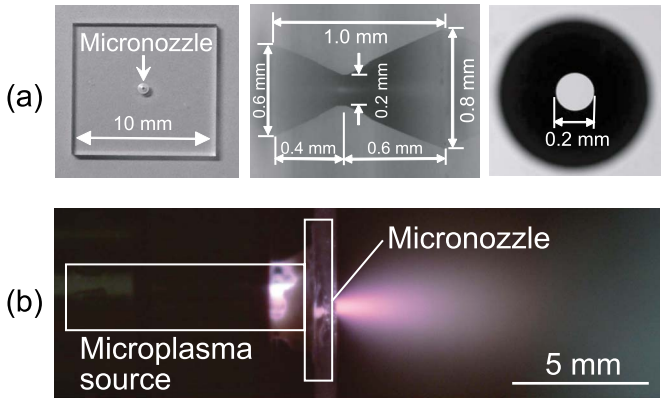

FIG. 10. (Color online) (a) Microscope image of the micronozzle fabricated in a 1-mm-thick quartz plate, which has an inlet, throat, and exit diameter similar to the configuration shown in Figs. 6 and 8. (b) Photograph image of the supersonic Ar plasma jet plume freely expanded into vacuum through the nozzle, taken under operating conditions of f=4 GHz, P_{in}=6 W, $\epsilon_d \approx 3.8$, Ar 50 SCCM (=1.5 mg/s), and p_0=31 kPa.

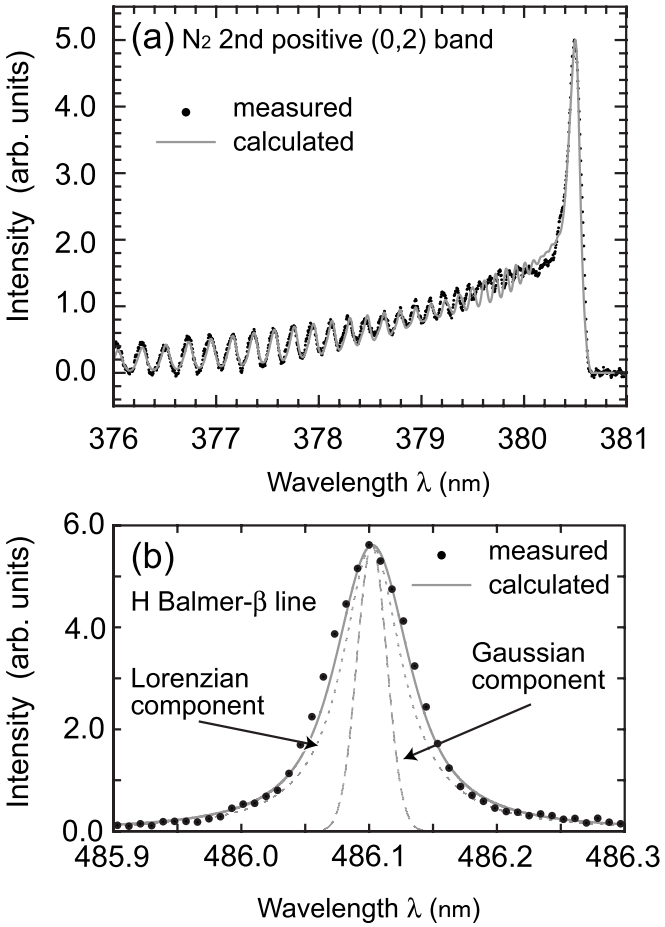

FIG. 12. (a) Vibronic spectrum of the N_2 second positive (0, 2) band at 380.4 nm, together with the spectrum theoretically calculated assuming the gas or rotational temperature $T_g \approx T_{rot}=890$ K. (b) Spectrum profile of the H Balmer β line at 486.1 nm, together with the fitting Voigt function curve that gives an FWHM of $\Delta\lambda_V=0.071$ nm. Also shown in (b) are the Gaussian and Lorentzian components of the Voigt profile with an FWHM of $\Delta\lambda_G \approx 0.027$ nm and $\Delta\lambda_L \approx 0.061$ nm, respectively, which gives the plasma electron density $n_e \approx 9.9\times10^{19}$ m^{-3}. These optical emissions were observed in the side-view direction through a small hole around the end of the microwave antenna or dielectric envelope (just upstream of the micronozzle inlet), under the same conditions as in Fig. 10(b) [$f=4$ GHz, $P_{in}=6$ W, $\epsilon_d \approx 3.8$, Ar 50 SCCM (=1.5 mg/s), and $p_0=31$ kPa].

slit width of 5 μm. In addition, a Langmuir probe was located in the plasma jet plume downstream of the nozzle exit to measure the plasma electron density therein,[27] where the probe was cylindrical with a tungsten wire 0.05 mm in diameter and 0.5 mm long.

IV. PLASMA CHARACTERISTICS

The gas/rotational temperature was measured by adding a small amount of N_2 and analyzing the optical emission spectrum of the N_2 second positive (0,2) band ($N_2C\ ^3\Pi_u,\ v'=0 \rightarrow B\ ^3\Pi_g,\ v''=2$) at 380.4 nm. Figure 12(a) shows a typical vibronic spectrum of the 380.4 nm N_2 band experimentally observed under the same conditions as in Fig. 10(b) ($f=4$ GHz, $P_{in}=6$ W, $\epsilon_d \approx 3.8$, Ar 50 SCCM, $p_0=31$ kPa), together with the spectrum theoretically calculated assuming the temperature $T_g \approx T_{rot}=890$ K.

The plasma electron density was measured by adding a small amount of H_2 and analyzing the Stark broadening of the H Balmer-β (H_β) spectral line at 486.1 nm. It is generally appreciated that the H_β line broadening consists of the instrumentation $\Delta\lambda_{instrum}$, Doppler $\Delta\lambda_{Doppler}$ (depending on T_g), pressure $\Delta\lambda_{pressure}$ (depending on T_g and p_0 or gas density n_g), and Stark broadening $\Delta\lambda_{Stark}$ (depending on n_e and T_e), where $\Delta\lambda_{instrum}$, $\Delta\lambda_{Doppler}$, $\Delta\lambda_{pressure}$, and $\Delta\lambda_{Stark}$ denote the respective full widths at half maximum (FWHMs);[45–48] the former two are given by the Gaussian profile and the latter two by the Lorentzian profile, which are then approximated by the Voigt function in total,

$$V(\lambda;\sigma,\gamma)=\int_{-\infty}^{\infty} G(\lambda';\sigma)L(\lambda-\lambda';\gamma)d\lambda', \tag{22}$$

where λ is the wavelength from the line center, $G(\lambda;\sigma)$ is the centered Gaussian component with an FWHM of $\Delta\lambda_G=2\sigma(2\ln 2)^{1/2}$, and $L(\lambda;\gamma)$ is the centered Lorentzian component with an FWHM of $\Delta\lambda_L=2\gamma$. The FWHM of the Gaussian component of the Voigt profile is given by

$$\Delta\lambda_G=(\Delta\lambda_{instrum}^2+\Delta\lambda_{Doppler}^2)^{1/2} \tag{23}$$

and that of the Lorentzian component by

$$\Delta\lambda_L=\Delta\lambda_{pressure}+\Delta\lambda_{Stark}. \tag{24}$$

In the present experiments, the Van der Waals broadening was only taken into account for pressure broadening, because the resonance broadening due to collisions between identical species could be neglected owing to a small amount of H_2 addition.

The instrumental broadening was estimated to be $\Delta\lambda_{instrum} \approx 0.025$ nm, as mentioned above in Sec. III. The Doppler, pressure, and Stark broadening was analyzed as in Ref. 48. Briefly, the respective FWHMs in nanometers are given by

$$\Delta\lambda_{Doppler}=7.16\times10^{-7}\lambda\sqrt{\frac{T_H}{M}}, \tag{25}$$

$$\Delta\lambda_{pressure} \approx \Delta\lambda_{Van\ der\ Waals} \approx 4.09\times10^{-12}\lambda^2(\alpha\langle R\rangle)^{2/5}\left(\frac{T_g}{\mu}\right)^{3/10}n_{Ar}, \tag{26}$$

$$\Delta\lambda_{Stark}=2.5\times10^{-10}a_{n'n}(n_e,T_e)n_e^{2/3}, \tag{27}$$

where λ is the wavelength of the emission line in nm, T_H is the temperature of emitters in K, M is the atomic weight of the emitter or H atom in atomic mass unit (amu). Moreover, α is the mean atomic polarizability of neutral perturbers or Ar atoms in cm^3, $\langle R\rangle$ is the parameter in cm^2 determined from atomic energy levels of the emitter, T_g is the gas temperature in K, μ is the emitter-perturber reduced mass in amu, and n_{Ar} is the neutral Ar gas density in cm^{-3}; $a_{n'n}$ is the parameter for the transition $n'-n$ of the emitter depending on n_e and T_e and n_e is the electron density in cm^{-3}. We took $\alpha \approx 11.08a_0^3$ from Ref. 49, $\langle R\rangle \approx 600a_0^2$ from Ref. 48, and $a_{n'n} \approx 0.08$ from Refs. 46, 50, and 51 in this study, where a_0 is the Bohr radius in centimeters.

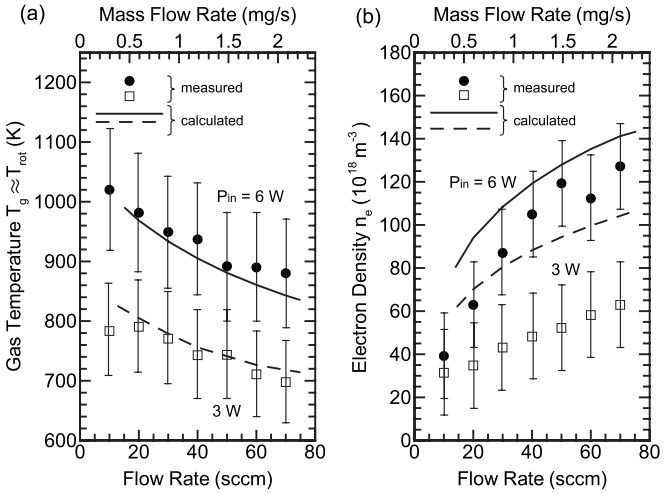

FIG. 13. (a) Plasma electron density n_e and (b) gas temperature $T_g \approx T_{rot}$ measured as a function of Ar gas flow rate for different microwave powers P_{in}, where changing the flow rate led to a change in pressure p_0 in the microplasma source as shown in Fig. 11. These data were taken under conditions of $f=4$ GHz and $\epsilon_d \approx 3.8$, with a small amount (0.2 SCCM) of additive gases of H_2 and N_2. Also shown in the figure are the curves of n_e and $T_g(=T_h)$ numerically simulated as in Figs. 4 and 7, where the data are those line averaged in the radial direction between the end of the antenna or dielectric envelope and the inlet of the micronozzle.

Figure 12(b) shows a typical profile of the H_β line spectrum at 486.1 nm experimentally observed under the same conditions as in Figs. 10(b) and 12(a), together with the best fitted curve of the Voigt function Eq. (22) that gives a FWHM of $\Delta\lambda_V \approx 0.071$ nm, where the fitting was performed according to the Marquardt–Levenberg method. In practice, $\Delta\lambda_G$ was calculated from Eq. (23) assuming the temperature $T_H \approx T_g \approx T_{rot}$ measured above and $\Delta\lambda_L$ was obtained from the best fit between the experimental spectrum and the Voigt profile calculated. Then, the Stark contribution $\Delta\lambda_{Stark}$ was found from Eq. (24), assuming the density $n_{Ar} \approx n_g \approx p_0/k_B T_g$. In the figure, $\Delta\lambda_G \approx 0.027$ nm ($\Delta\lambda_{instrum} \approx 0.025$ nm and $\Delta\lambda_{Doppler} \approx 0.010$ nm) gave $\Delta\lambda_L \approx 0.061$ nm ($\Delta\lambda_{pressure} \approx 0.010$ nm), which in turn gave $\Delta\lambda_{Stark} \approx 0.051$ nm, and thus $n_e \approx 9.9 \times 10^{19}$ m^{-3}, assuming $T_g \approx 890$ K and $p_0 \approx 30$ kPa. It should be noted that the accuracy of the electron density determined from the Stark broadening relies on the spectral resolution of the measurement system and also on the assumption of analysis of the spectral line broadening; in practice, the present accuracy was estimated to be about $\pm 20\%$ at $P_{in}=6$ W, primarily owing to the resolution $\Delta\lambda_{instrum}$ of the spectrometer system employed.

Figure 13 shows the plasma electron density n_e and gas/rotational temperature $T_g \approx T_{rot}$ measured as a function of Ar gas flow rate for different microwave powers P_{in} ($f=4$ GHz, $\epsilon_d \approx 3.8$), where changing the flow rate led to a change in pressure p_0 or gas density n_g in the microplasma source as shown in Fig. 11. The electron density was in the range $n_e \approx (8-16) \times 10^{19}$ m^{-3}, being consistent with the Langmuir probe measurements in the supersonic plasma free jet downstream of the nozzle.[27] Moreover, the gas temperature was in the range $T_g \approx T_{rot} \approx 700-1000$ K. The temperature $T_g \approx T_{rot}$ was observed to increase with increasing P_{in} and to decrease with increasing flow rate (or with increasing p_0 or n_g in the plasma source). On the other hand, the density n_e was observed to increase with increasing P_{in} and flow rate. Also shown in the figure are the curves of n_e and $T_g(=T_h)$ numerically simulated as in Figs. 4 and 7, where the data are those line-averaged in the radial direction between the end of the microwave antenna or dielectric envelope and the inlet of the nozzle, indicating that the experiments were in agreement with the numerical analysis.

V. THRUST PERFORMANCE

The thrust performance is calculated as[44,52]

$$F_t = 2\pi \int_0^{r_{ex}} (\rho u^2 + p) r dr, \tag{28}$$

$$I_{sp} = F_t \left(2\pi g \int_0^{r_{ex}} \rho u r dr \right)^{-1} = \frac{F_t}{\dot{m} g}, \tag{29}$$

based on the numerical analysis in Sec. II, where F_t is the thrust (or the reaction force to propel spacecraft) and I_{sp} is the specific impulse (or the fuel efficiency of thrusters). In these equations, r_{ex} denotes the exit radius of the nozzle, ρ the mass density, u the exhaust flow velocity in the axial direction, p the pressure, $\dot{m}$ the mass flow rate, and g the gravitational constant. Note that F_t consists of the momentum and pressure thrust. The pressure thrust is usually neglected owing to its less contribution to the total thrust. However, reducing the size of the nozzle results in underexpanded gas/plasma flows inside the nozzle owing to highly viscous flows therein, as mentioned earlier in Sec. II C, so that the pressure thrust should be taken into account in the present microplasma thruster.[25,28]

The experimental setup for thrust measurement has been detailed elsewhere,[28] which was newly developed for microthrusters of $F_t \leq 1$ mN, consisting of a pendulum-type stand for cold-gas operation and a target-type stand for both cold-gas and plasma-discharge operations. In the former, the thruster itself was hung; on the other hand, in the latter, a small concave cylindrical target block was hung downstream of the nozzle exit with the thruster fixed tightly and the gas/plasma plume ejected from the thruster struck the target mounted at one end of the pendulum with some weights being at the other end for balance. Here, the target employed was a small Faraday cuplike one made of Teflon to suppress the effects of reflected particles of the jet plume striking the target. A small displacement of $\Delta X < 0.1$ mm in operation was measured by using a laser displacement gauge having a resolution of $\Delta x < 0.1$ μm. It should be noted that the accuracy of the present thrust measurement was estimated to be about $\pm 10\%$, relying primarily on mechanical issues of the measurement system such as effects of friction of the knife edge on the rotational axis and effects of the reflected jet plume particles on the target.

Figure 14 shows the thrust performance (thrust F_t, specific impulse I_{sp}) measured and calculated as a function of Ar gas flow rate for different microwave input powers P_{in}, where $P_{in}=0$ W corresponds to the cold-gas operation with-

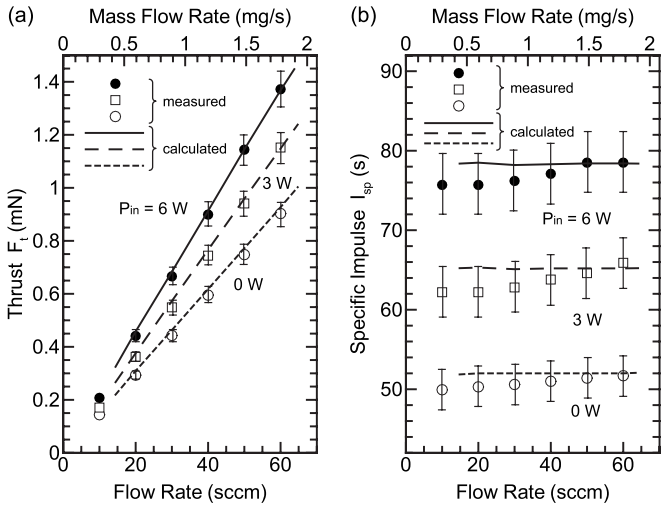

FIG. 14. Thrust performance [(a) thrust F_t and (b) specific impulse I_{sp}] measured as a function of Ar gas flow rate for different microwave powers P_{in} under the same conditions as in Fig. 13 (f=4 GHz, $\epsilon_d \approx 3.8$). Here, P_{in}=0 W corresponds to the cold-gas operation without plasma discharge. Also shown in the figure are the curves of F_t and I_{sp} calculated from the numerical analysis as in Figs. 6 and 8.

out plasma discharge. The measurements showed that the thrust performance was enhanced with the discharge on and with increasing P_{in} and that the thrust and specific impulse were typically $F_t \approx 1.4$ mN and $I_{sp} \approx 80$ s, respectively, with the thrust efficiency $\eta_t \approx 8.7\%$ at $P_{in}=6$ W and a flow rate of 60 SCCM (1.8 mg/s). In practice, a good agreement was obtained between the experiments and numerical analysis, giving $F_t \approx 0.2-1.4$ mN, $I_{sp} \approx 50-80$ s, and $\eta_t \approx 2-12\%$ at $P_{in} \leq 6$ W and gas flow rates of 10–60 SCCM.

VI. CONCLUSIONS

A microplasma thruster has been developed of electrothermal type using azimuthally symmetric microwave-excited microplasmas, which consisted of a microplasma source and micronozzle. The plasma source was made of a dielectric chamber 1.5 mm in diameter and 10 mm long covered with a metal grounded, having a metal rod antenna on axis covered with a dielectric envelope, to produce high temperature plasmas at around atmospheric pressures. The nozzle was a converging-diverging type (Laval nozzle) 1 mm long with a throat 0.2 mm in diameter, converting high thermal energy of plasmas into directional kinetic energy of supersonic plasma flows to obtain the thrust required. The feed or propellant gas employed was Ar at pressures of 10–50 kPa with flow rates of 10–70 SCCM and the surface wave-excited plasmas were established by 4.0 GHz microwaves at input powers of $P_{in} \leq 6$ W. Numerical analysis was made for the plasma and flow properties in the microplasma source and micronozzle by developing a self-consistent numerical model, where a two-temperature fluid model was applied to the entire region through the plasma source to nozzle. In the former, the electromagnetic model based on the FDTD approximation was also employed for analysis of microwaves interacting with plasmas. Numerical results revealed the spatially nonuniform distribution of plasma and flow parameters in the microplasma source: the absorbed power density, plasma density, and gas temperature are maximum at around the end of the microwave antenna or dielectric envelope (just upstream of the inlet of the micronozzle), which is preferred for a thruster of electrothermal type using the converging-diverging nozzle. The numerical results also indicated that the supersonic flow in the micronozzle is heavily affected by viscous dissipation in thick boundary layers and that the deceleration of supersonic flow occurs at low gas flow rates and high input powers.

Optical emission spectroscopy was employed with a small amount of additive gases of H_2 and N_2 to measure the plasma electron density and gas temperature in the microplasma source at around the end of the antenna or dielectric envelope. The analysis of the Stark broadening of H Balmer H_β spectral line and the vibronic spectrum of N_2 second positive (0, 2) band indicated that the electron density was in the range $n_e \approx (3-12) \times 10^{19}$ m^{-3} and the gas or rotational temperature was in the range $T_g \approx T_{rot} \approx 700-1000$ K. In practice, n_e was found to increase with increasing microwave power and flow rate (or increasing pressure or gas density in the plasma source), while T_g increased with increasing power and decreased with increasing flow rate. The thrust performance was also measured by developing a microthrust stand with a combination of target and pendulum methods, giving a thrust in the range $F_t \approx 0.2-1.4$ mN, a specific impulse in the range $I_{sp} \approx 50-80$ s, and a thrust efficiency in the range $\eta_t \approx 2-12\%$. The thrust performance was found to increase with the discharge on and with increasing microwave power. These experimental results were consistent with those of numerical analysis, depending on microwave power and gas flow rate. The micro plasma thruster presently developed would be applicable to attitude-control and station-keeping maneuver for microspacecraft of <10 kg. Further investigations are now in progress with lighter feed or propellant gases such as H_2 and He.

ACKNOWLEDGMENTS

This work was supported in part by a Grant-in-Aid for Scientific Research from the Japan Society for the Promotion of Science and in part by the 21st century Center of Excellence (COE) program of the Ministry of Education, Culture, Sports, Science and Technology.

The authors would like to thank Y. Ichida and S. Kitanishi for assistance with experiments.

[1] E. Y. Robinson, H. Helvajian, and S. W. Janson, Aerosp. Am. **Oct.**, 38 (1996).
[2] H. Helvajian and S. W. Janson, in *Microengineering Aerospace Systems*, edited by H. Helvajian (AIAA, Reston, 1999), Chap. 2.
[3] J. Mueller, in *Micropropulsion for Small Spacecraft*, edited by M. M. Micci and A. D. Ketsdever (AIAA, Reston, 2000), Chap. 3.
[4] J. R. Wilson, Aerosp. Am. **Feb.**, 34 (2003).
[5] M. Tajmar, *Advanced Space Propulsion Systems* (Springer, Vienna, 2004), Chap. 2.
[6] J. Sethian, in *MEMS and Microstructures in Aerospace Applications*, edited by R. Osiander, M. A. G. Darrin, and J. L. Champion (CRC, Boca Raton, 2005), Chap. 11.
[7] H. Horisawa, K. Onodera, T. Noda, and I. Kimura, Vacuum **80**, 1244 (2006).

[8]H. Okamoto and M. Nishida, Trans. Jpn. Soc. Aeronaut. Space Sci. **48**, 187 (2006).
[9]T. Deconinck, S. Mahadevan, and L. L. Raja, IEEE Trans. Plasma Sci. **36**, 1200 (2008).
[10]P. S. Kothnur and L. L. Raja, J. Appl. Phys. **97**, 043305 (2005).
[11]T. Ito and M. A. Cappelli, Appl. Phys. Lett. **89**, 061501 (2006).
[12]T. Ito, N. Gascon, W. S. Crawford, M. A. Cappelli, and J. Propul, Power **23**, 1068 (2007).
[13]H. Kataharada, Y. Takao, N. Yamamoto, H. Ijiri, and H. Nakashima, Thin Solid Films **506–507**, 605 (2006).
[14]N. Yamamoto, S. Kondo, T. Chikaoka, H. Nakashima, and H. Masui, J. Appl. Phys. **102**, 123304 (2007).
[15]M. A. Kemp and S. D. Kovaleski, J. Appl. Phys. **100**, 113306 (2006).
[16]M. A. Kemp and S. D. Kovaleski, IEEE Trans. Plasma Sci. **36**, 356 (2008).
[17]A. Dunaevsky, Y. Raitses, and N. J. Fisch, Appl. Phys. Lett. **88**, 251502 (2006).
[18]M. Tajmar, A. Genovese, W. Steiger, and J. Propul, Power **20**, 211 (2004).
[19]S. Castro and R. Bocanegra, Appl. Phys. Lett. **88**, 123105 (2006).
[20]J. Schein, N. Qi, R. Binder, M. Krishnan, J. K. Ziemer, J. E. Polk, and A. Anders, Rev. Sci. Instrum. **73**, 925 (2002).
[21]T. Moeller and Y. K. Chang, Aerosp. Sci. Technol. **11**, 481 (2007).
[22]M. Keidar, I. D. Boyd, J. Luke, and C. Phipps, J. Appl. Phys. **96**, 49 (2004).
[23]J. Aoyagi, M. Mukai, Y. Kamishima, T. Sasaki, K. Shintani, H. Takegahara, T. Wakizono, and M. Sugiki, Vacuum **83**, 72 (2008).
[24]E. L. Antonsen, R. L. Burton, G. A. Reed, and G. G. Spanjers, Rev. Sci. Instrum. **77**, 103107 (2006).
[25]Y. Takao and K. Ono, Plasma Sources Sci. Technol. **15**, 211 (2006).
[26]Y. Takao, K. Ono, K. Takahashi, and Y. Setsuhara, Thin Solid Films **506–507**, 592 (2006).
[27]Y. Takao, K. Ono, K. Takahashi, and K. Eriguchi, Jpn. J. Appl. Phys., Part 1 **45**, 8235 (2006).
[28]Y. Takao, K. Eriguchi, and K. Ono, J. Appl. Phys. **101**, 123307 (2007).
[29]T. Takahashi, Y. Takao, K. Eriguchi, and K. Ono, in Proceedings of the 30th International Electric Propulsion Conference, Florence, Italy, September 2007, Paper No. IEPC-2007-29.
[30]Y. Takao, T. Takahashi, K. Eriguchi, and K. Ono, Pure Appl. Chem. **80**, 2013 (2008).
[31]T. Takahashi, Y. Takao, K. Eriguchi, and K. Ono, J. Phys. D **41**, 194005 (2008).
[32]M. Tuda and K. Ono, J. Vac. Sci. Technol. A **16**, 2832 (1998).
[33]M. Tuda, K. Ono, H. Ootera, M. Tsuchihashi, M. Hanazaki, and T. Komemura, J. Vac. Sci. Technol. A **18**, 840 (2000).
[34]H. Kousaka and K. Ono, Jpn. J. Appl. Phys., Part 1 **41**, 2199 (2002).
[35]H. Kousaka and K. Ono, Plasma Sources Sci. Technol. **12**, 273 (2003).
[36]J. T. Gudmundsson and E. G. Thorsteinsson, Plasma Sources Sci. Technol. **16**, 399 (2007).
[37]M. A. Lieberman and A. J. Lichtenberg, *Principles of Plasma Discharges and Materials Processing*, 2nd ed. (Wiley, New York, 2005), Chap. 3.
[38]K. Tachibana, Phys. Rev. A **34**, 1007 (1986).
[39]F. Kannari, M. Obara, and T. Fujioka, J. Appl. Phys. **57**, 4309 (1985).
[40]L. M. Biberman, V. S. Vorob'ev, and I. T. Yakubov, *Kinetics of Nonequilibrium Low-Temperature Plasmas* (Consultants Bureau, New York, 1987), Chap. 2.
[41]S. Yoon and A. Jameson, AIAA J. **26**, 1025 (1988).
[42]D. R. Miller, in *Atomic and Molecular Beam Methods*, edited by D. Scoles, D. Bassi, U. Buck, and D. Laine (Oxford University Press, New York, 1988), Vol. 1, Chap. 2.
[43]H. W. Liepmann and A. Roshko, *Elements of Gas Dynamics* (Wiley, New York, 1957), Chap. 2.
[44]G. P. Sutton and O. Biblarz, *Rocket Propulsion Elements* (Wiley, New York, 2001), Chap. 3.
[45]H. R. Griem, *Plasma Spectroscopy* (McGraw-Hill, New York, 1964), Chap. 4.
[46]H. R. Griem, *Spectral Line Broadening by Plasmas* (Academic, New York, 1974), Chap. 3 and Appendix I.
[47]H. R. Griem, *Principles of Plasma Spectroscopy* (Cambridge University Press, Cambridge, 1997), Chaps. 4 and 10.
[48]Q. Wang, I. Koleva, Y. M. Donnelly, and D. J. Economou, J. Phys. D **38**, 1690 (2005).
[49]J. Mitroy and M. W. Bromley, Phys. Rev. A **68**, 5201 (2003).
[50]M. A. Gigosos and V. Gardenoso, J. Phys. B **29**, 4795 (1996).
[51]J. M. Luque, M. D. Calzada, and M. Saez, J. Phys. B **36**, 1573 (2003).
[52]G. Wirsig, in *Space Propulsion Analysis and Design*, edited by R. W. Humble, G. N. Henry, and W. J. Larson (McGraw-Hill, New York, 1995), Chap. 3.